Glancing-angle deposition of magnetic in-plane exchange springs

Andreas Frisk,[1,†] Barat Achinuq,[2,†] David G. Newman,[3] Maciej Dąbrowski,[3] Robert J. Hicken,[3] Gerrit van der Laan,[1] and Thorsten Hesjedal[2,*]

[1] *Diamond Light Source, Harwell Science and Innovation Campus, Didcot, Oxfordshire OX11 0DE, United Kingdom*

[2] *Department of Physics, University of Oxford, Parks Road, Oxford OX1 3PU, United Kingdom*

[3] *Department of Physics and Astronomy, University of Exeter, Stocker Road, Exeter, Devon EX4 4QL, United Kingdom*

(Received 21 July 2023; revised 8 September 2023; accepted 25 September 2023; published 10 October 2023)

Magnetic exchange springs (ESs) are composed of exchange-coupled hard and soft magnetic layers, i.e., layers with high and low anisotropy, respectively. The moments in the soft layer can be wound up by applying an external field, which has to be smaller than the anisotropy field of the hard layer. Alternatively, an ES can be realized by biasing the soft magnetic layer by two adjacent hard magnetic layers with different magnetic anisotropy directions. We have fabricated an ES layer stack by magnetron sputter deposition. As the hard magnetic bottom layer, we used epitaxial FePt $L1_0$, and as the top layer Co with both layers having different in-plane easy axes. These hard layers pin the moments of a soft permalloy ($Ni_{81}Fe_{19}$) layer sandwiched between them, winding up an ES at remanence. The anisotropy of the polycrystalline top Co layer was engineered by glancing-angle deposition to have in-plane easy axis anisotropy perpendicular to the easy direction of the bottom layer. Using soft x-ray spectroscopy and magneto-optical measurements, we found the in-plane ES to extend from the soft layer into the top layer of our FePt/permalloy/Co trilayer structure.

DOI: 10.1103/PhysRevApplied.20.044027

I. INTRODUCTION

Magnetic exchange spring (ES) materials are composed of exchange-coupled hard and soft magnetic layers, and were developed in an attempt to create permanent magnets with higher maximum energy products $(BH)_{max}$ of the magnetic induction intensity B and the magnetic field intensity H [1]. Since their initial proposal, other advantages and possible applications beyond permanent magnets have emerged, such as magnetic memories, for which the combination of high coercivities and low switching fields are ideal for low-power devices. In particular, by using microwave-assisted switching of the hard layer via the excitation of spin waves in the soft layer [2,3], ES systems are attractive for, e.g., microwave-assisted magnetic recording (MAMR) devices [4,5].

While for winding up an exchange spring, the application of an external field is commonly required, we show here that it is possible to wind up an exchange spring at remanence by sandwiching a soft layer between two hard layers with different in-plane easy axes (which should ideally be separated by 90°). To achieve different anisotropies in a magnetic heterostructure, we control the magnetic anisotropy directions of the two hard layers by two different mechanisms. While the bottom layer is epitaxially grown, and its magnetic anisotropy thus controlled by its crystalline orientation, the magnetic anisotropy of the top layer is controlled by imprinting the anisotropy axis using glancing angle deposition (GLAD) [6,7]. The ability of GLAD to control the magnetic anisotropy direction of a thin film is an established technique [7–9], whereby the magnetic easy axis can be tuned to be perpendicular to the imprinting axis [8,9].

*Thorsten.Hesjedal@physics.ox.ac.uk

†These authors contributed equally to this work.

II. EXPERIMENTAL DETAILS

A. Basic zero-field exchange spring concept and anisotropy engineering

The basic concept of an exchange spring system is illustrated in Fig. 1. Let us start with a two-layer system, with one of the ferromagnetic layers being a hard layer with

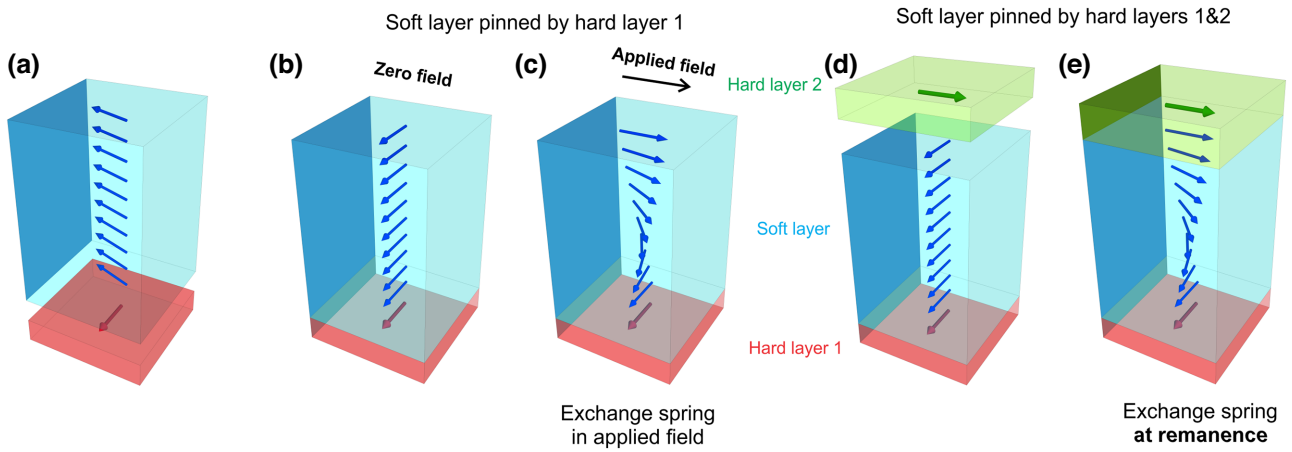

FIG. 1. Illustration of magnetic exchange springs in bi- and trilayer systems, composed of magnet hard (red) and soft layers (blue). (a) When a hard and a soft layer are combined at zero field, the soft layer magnetization will follow that of the hard layer (b). (c) By applying a field, the soft layer magnetization further away from the interface will align with the field, while the magnetization close to the interface remains pinned, setting up an exchange spring. (d) Alternatively, the need for an applied field can be overcome by adding a second hard layer (green), with an anisotropy axis perpendicular to that of the first layer, which sets up the spring at remanence (e).

large magnetic anisotropy and the other a soft layer with low anisotropy [Fig. 1(a)]. When they are brought into contact, the soft layer magnetization reorients in the direction of the hard layer [Fig. 1(b)]. If such a system undergoes a magnetization reversal, the soft layer starts switching as soon as the field is applied, leading to a continuous rotation of the soft layer magnetization from the pinned direction at the interface with the exchange-coupled hard layer, to the field direction at the top, setting up an ES [Fig. 1(c)]. In order to achieve an ES at remanence, a second hard layer can be added, whose hard axis is perpendicular to that of the first hard layer [Fig. 1(d)]. Through exchange coupling at the respective interfaces, an ES is set up in the soft layer at remanence [Fig. 1(e)]. In order to achieve this behavior, the anisotropy of the two hard layers has to be controlled. One solution is to make layers that are governed by different anisotropy mechanisms, e.g., controlling the first layer via substrate constraints and the second via anisotropy engineering. In the GLAD process, several parameters affect the anisotropy of a film, such as thickness, glancing angle, and substrate effects [7], and our goal in this work has been to imprint the anisotropy and stabilize a 90° spring at remanence.

B. Sample growth

The heterostructures were grown in a home-built magnetron sputter deposition system (base pressure $< 3 \times 10^{-8}$ mbar), capable of glancing angle deposition (which is described in detail in Ref. [7]).

The angles relevant for the GLAD growth are α, the incident deposition angle onto the sample, and β, the in-plane direction of deposition and thus the axis of imprinted anisotropy (see Fig. 2, top left for side and top views illustrating α and β, respectively). Both α and β can be controlled via the polar and azimuthal substrate rotations, respectively.

The FePt/Py/Co trilayers (Py $= Ni_{81}Fe_{19}$) were grown on MgO(110) substrates, as illustrated in Fig. 2, using 99.999% pure Ar as the sputtering gas at a pressure of approximately 2×10^{-3} mbar. The MgO(110) substrates were annealed in the growth chamber at 650 °C for 3 h. While keeping the substrate at 650 °C (all temperatures are thermocouple readings), Fe and Pt were co-deposited with individual deposition rates giving a nominal composition of FePt and a total deposition rate of 0.3 Å/s (100 Å nominal thickness). This layer was deposited at normal incidence for co-sputtering conditions, resulting in epitaxial growth of FePt(110) [10]. Subsequently, the temperature was decreased to 150 °C and a Py layer was deposited at normal incidence. A slightly higher deposition rate of 0.62 Å/s was used for the Py layer (50 Å nominal thickness), with intention to induce disorder. Note that with increasing deposition rate, the adatom mobility is reduced, leading to disorder [11]. Next, while keeping the temperature at 150 °C, a Co layer was deposited under GLAD conditions with $\alpha_{Co} = 80°$ and $\beta_{Co} = 0°$. The aim was to induce a hard axis along the $\beta = 0°$ direction. An effective deposition rate of 0.13 Å/s was used, which corresponds to a normal incidence deposition rate of 0.35 Å/s (300 Å nominal thickness). Finally, the trilayer was capped with a thin Pt layer (30 Å nominal thickness) to protect it against oxidation.

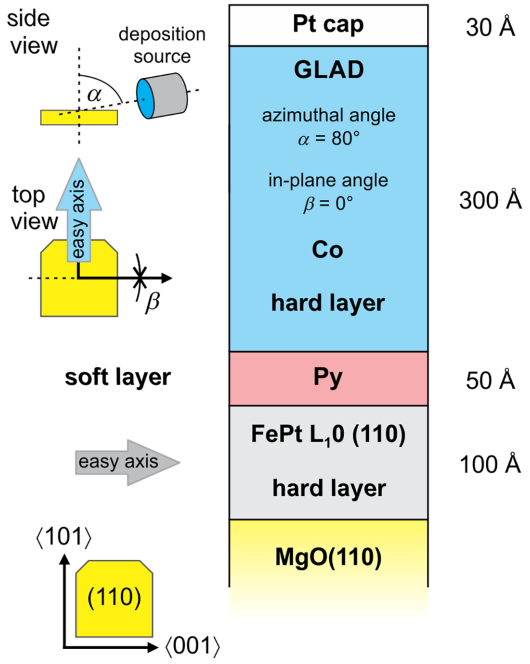

FIG. 2. Illustration of the thin-film stack. Starting with the MgO(110) substrate, an epitaxial $L1_0$ FePt layer is grown on top, which has an easy axis of magnetization as indicated. The following Py layer should ideally be polycrystalline and exhibit low magnetic anisotropy (soft layer). Finally, a Co layer is deposited as the second hard magnetic layer. By using GLAD at an in-plane angle of $\beta = 0°$ and an incident deposition angle of $\alpha = 80°$, the easy axis should ideally be in-plane and perpendicular to the easy axis of the FePt layer. Both deposition angles are illustrated in the side and top views on the left-hand side. The whole structure is capped with Pt to prevent from oxidation.

C. Sample characterization

1. XRR and XRD

A Rigaku Smart Lab X-ray diffractometer was used to measure X-ray reflectivity (XRR) and various types of x-ray diffraction (XRD) patterns using Cu $K\alpha$ radiation. Out-of-plane ω-2θ as well as in-plane ϕ-$2\theta_\chi$ diffractograms were recorded. Also, in-plane ϕ scans were carried out to confirm the epitaxial relationship between the FePt $L1_0$ layer and the MgO(110) substrate. XRR scans were measured to determine the layer thicknesses, densities, and roughnesses, obtained by fitting the data using GenX [12].

2. TEM

For TEM imaging, cross-section samples were prepared by focused ion beam (FIB) milling using a JEOL JIB-4700F multibeam system. Before the FIB process, the samples were *ex situ* sputter coated with a Au layer to reduce possible charging effects and to protect the surface from ion beam damage. Before starting the milling procedure in the FIB, an approximately 300-nm-thick sacrificial Pt layer was deposited using the electron beam to protect the film from Ga ion implantation, followed by an approximately 3-μm-thick Pt layer using the Ga beam to further protect the surface from any implantation and damage during the FIB process. TEM images of the samples were recorded using a JEOL JEM-2100 TEM operating at 200 keV.

3. MOKE

A NanoMOKE3 from Durham Magneto Optics was used to record in-plane hysteresis loops via the longitudinal magneto-optical Kerr effect (*L*MOKE). The loops were measured at different in-plane angles φ_H in the range from 0° to 360°. The MOKE system uses a 660-nm wavelength laser with an incident angle of 30° from the surface normal, which gives a penetration depth less than approximately 300 Å, i.e., only the thicker Co top layer (nominal thickness 300 Å + 30 Å Pt cap) contributes to the MOKE signal. Note that the instrument software performs preprocessing of the data by subtracting a linear background.

4. VSM

In-plane hysteresis loops were measured at different in-plane angles φ_H in the range between 0° to 360° using room-temperature vibrating sample magnetometry (VSM). The MicroSense VSM system is capable of bias fields of up to 1.8 T. The samples were mounted on a quartz rod, which can be rotated to cover the full ϕ_H range. The data points were usually averaged 5 times to improve the signal-to-noise ratio.

5. XMCD

X-ray magnetic circular dichroism (XMCD) experiments were carried out at beamline I10 at the Diamond Light Source, UK, and at beamline 6.3.1 at the Advanced Light Source, USA. Element-resolved magnetization loops were recorded by measuring the intensity difference of the right- and left-circularly polarized light at the L_3 edge of Fe, Co, and Ni in varying applied magnetic field. The absorption was measured simultaneously by total electron yield (TEY) detection, and, in transmission, by luminescence yield (LY) detection. TEY has a probing depth of 3–5 nm [13]. On the other hand, LY mode probes the entire stack of the heterostructure. In LY, the transmitted x rays that are not absorbed in the sample stack give rise to x-ray-excited optical luminescence in the MgO substrate. The emitted optical photons exit through a hole in the back of the sample holder and are detected by a photodiode [14]. The x rays were incident on the sample at an angle of 30° from the sample surface, giving sensitivity to the in-plane magnetization component. The intensity of the XMCD spectra in LY mode, together with the magnetization measured with VSM, was used to scale the respective Fe, Co,

and Ni loops to allow for their comparison. Both types of measurements were done at selected in-plane angles φ_H.

D. Micromagnetic simulations

The micromagnetic behavior of the thin-film structures was simulated using the Ubermag simulation package [15–17]. For the simulations, we took the exchange interaction, the exchange energy for each of the interfaces and the respective uniaxial and cubic anisotropies of the films into account. For details, please consult the Ubermag documentation [18]. The heterostructure was modeled by a slab measuring 1000×1000 Å^2 in area, using a discretization cell size of $40 \times 40 \times 5$ Å^3, and the individual layer thicknesses obtained from XRR fits. The FePt and Co layers were assumed to have uniaxial anisotropy with the anisotropy axes pointing along the (in-plane) FePt [001] direction and perpendicular to it (also in-plane), respectively. The Py layer was assumed to have cubic anisotropy, with the easy axes pointing along the FePt [001] and [100] directions. Note that Py is growing epitaxially on FePt, sharing the crystallographic orientations with the FePt layer. Further, demagnetization (with demagnetization field $\mathbf{H}_d$) was taken into account. The total energy was minimized for varying applied field values and in-plane angles to obtain the hysteresis loop. At each field point, the average magnetization in each layer was calculated, revealing layer-resolved and element-resolved loops in addition to the averaged behavior for the entire stack. This allows for the direct comparison with the measured data obtained with the different experimental methods. The values for the saturation magnetization M_S^{FePt} (1.01×10^6 A/m), M_S^{Py} (4.42×10^5 A/m), M_S^{Co} (1.41×10^6 A/m), the anisotropy constants K_U^{FePt} (1×10^6 J/m^3), K_C^{Py} (-1×10^3 J/m^3), K_U^{Co} (4×10^4 J/m^3), and the exchange energy constants A^{FePt} (1.0×10^{-12} J/m), A^{Py} (1.0×10^{-11} J/m), and A^{Co} (3.1×10^{-11} J/m) were obtained by manually fitting the simulated loops to the corresponding measured loops. Note that the anisotropy axis of FePt is along the [001] direction (i.e., in plane) and that of Co 90° perpendicular to it (also in plane). For Py, a weak cubic anisotropy was assumed [19] (axes parallel to FePt [001] and [100]), which is reasonable given that Py is growing epitaxially on FePt and shares the crystallographic orientations. Finally, the evolution of the spin structure throughout the thickness of the system was obtained by plotting the direction of the magnetic moments lying along the (in-plane) symmetry axis.

III. RESULTS AND DISCUSSION

A. Structure

The layer thicknesses were confirmed by XRR (Fig. 3), giving the following thicknesses (uncertainties): $d_{\mathrm{FePt}} = 118(4)$, $d_{\mathrm{Py}} = 57(23)$, $d_{\mathrm{Co}} = 285(25)$, and $d_{\mathrm{Pt}} = 24(6)$ Å,

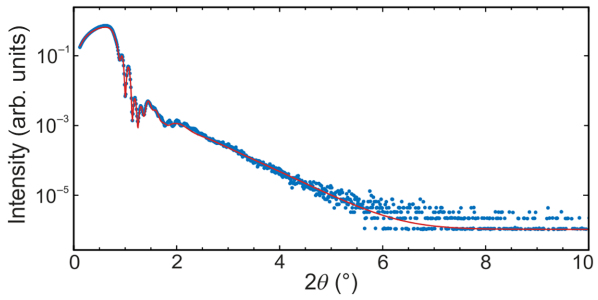

FIG. 3. XRR of the sample, revealing a high roughness. The solid lines are fits to the data using GenX [12]. From the XRR, the thickness of the sample was determined to be FePt(118)/Py(57)/Co(285)/Pt(24) (thicknesses in Å).

agreeing reasonably well with the target thicknesses of 100, 50, 300, and 30 Å, respectively. The corresponding interfacial roughnesses (uncertainties) were determined to be $\sigma_{\mathrm{FePt}} = 17(3)$, $\sigma_{\mathrm{Py}} = 19(4)$, $\sigma_{\mathrm{Co}} = 28(10)$, and $\sigma_{\mathrm{Pt}} = 28(2)$ Å, respectively. The FePt layer has a sizeable roughness, governing the roughnesses of the subsequent layers as well. Moreover, the roughness of the Co layer is further increased due to the GLAD deposition process.

In- and out-of-plane XRD measurements (Figs. 4 and 5) confirm the epitaxial growth of FePt(110) on MgO(110) with the epitaxial relationship FePt[001](110) ∥ MgO[001](110). The reflections of FePt(001), (110), and (101) are visible, which confirms the successful growth of the chemically ordered $L1_0$ phase [10] with the c axis ([001] direction) in plane. We further find the FePt(202) reflection to be split [see Fig. 5(b)], which could be due to twinning or due to the presence of both the $L1_0$ and A1 phase. The long-range order parameter $S_{110} = \sqrt{(I_{\mathrm{exp}}^{110}/I_{\mathrm{exp}}^{220})/(I_{\mathrm{theo}}^{110}/I_{\mathrm{theo}}^{220})}$, where $I_{\mathrm{theo}}^{hkl} = |F_{hkl}|^2 A_{hkl} LP_{hkl}$, with F_{hkl} the structure factor, A_{hkl} is the absorption factor, and LP_{hkl} is the Lorentz polarization factor [20], was calculated to $S_{110} = 0.17$. This rather low value (a fully ordered system would have $S = 1$) shows that the chemical order of the tetragonal $L1_0$ phase is incomplete. Previous reports found that FePt deposited on a Pt or Au seed layer on MgO(110) also grow in the $L1_0$ structure with its c axis oriented in plane [10,21–25], however, the c axis was reported to be canted out of the film plane when deposited directly on MgO(110) [26,27].

The correlation length ξ (calculated using the Scherrer equation [28] with a prefactor of 1) of the FePt(220) reflection of $\xi \approx 126$ Å is larger than the layer thickness, indicating a good layer quality. Further, the XRD data shows that the Py layer is growing epitaxially on FePt with the (220) reflection visible, and also having a correlation length larger than the layer thickness of approximately 50 Å. The three reflections, which can be attributed to Co, are the hexagonal (0002) reflection, as well as the (111) and (222) reflections of fcc Co (or possibly CoPt).

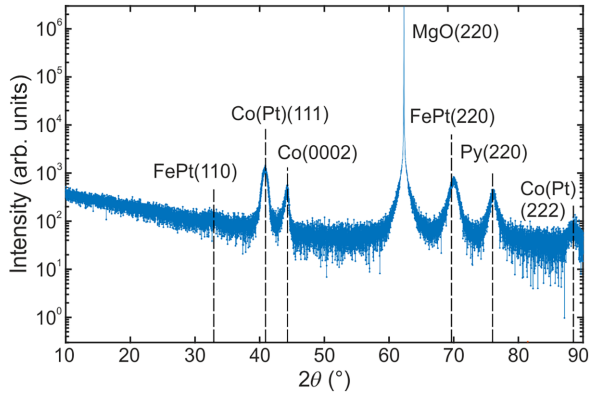

FIG. 4. Out-of-plane ω-2θ XRD scan of the sample with Cu $K\alpha$ radiation.

The quality of the interfaces, and the structural effects of the GLAD process on the morphology of the Co film were further investigated using TEM. Figure 6(a) shows a bright-field TEM image of the interfaces. The FePt interfaces with MgO and Py can be clearly distinguished. Whereas the interface between FePt and Py is abrupt, the interface with MgO appears distorted. The Co layer shows the anticipated columnar growth, with an inclination angle resulting from the GLAD process of roughly 70°. This is in good agreement with the value expected from the tangent rule, $\tan(\alpha_{\mathrm{Co}}) \approx 2\tan(\gamma)$ [29], of $\gamma = 71^\circ$ for $\alpha_{\mathrm{Co}} = 80^\circ$ used in the GLAD deposition. Figure 6(b) shows a high-resolution TEM image of the metallic layers, revealing epitaxial growth of the FePt and Py layers with a large density of stacking faults, which extend from the MgO substrate all the way into the Co layer. The fact that the MgO surface appears rough and that the stacking faults can be traced back to the oxygen-deficient areas of the substrate means that the high-temperature substrate preparation is their most likely cause. Figure 6(c) shows the diffractogram obtained from (b), revealing that the FePt and Py layers are highly epitaxial, consistent with the XRD measurements. Note that as the TEM images were taken looking down the [101] zone axis, no further insight could be gained with regards to whether the splitting of the FePt(202) reflection in XRD [Fig. 5(b)] is due to twinning or due to the presence of both the $L1_0$ and A1 phase.

B. Magnetization

The magnetization of the FePt/Py/Co layer stack was investigated using a set of complementary tools, each giving insight into specific aspects of the magnetic behavior. For example, while VSM magnetometry probes the magnetic response of all layers combined, MOKE with its limited penetration depth of <300 Å only probes the top layer (here Co), while XMCD in LY mode probes element-selectively the various layers of the stack. Note that, as Fe is present in both the FePt and Py layers, the XMCD signal will show a combined response of these two layers, while the Ni and Co signals are specific to the Py and Co layers, respectively.

The bottom hard magnetic FePt layer, with its dominating, chemically disordered $L1_0$ phase, shows a strong magnetic anisotropy with the easy axis along the in-plane [001] direction. We refer to this direction as $\phi_H = 0^\circ$. Figure 7 shows the (in-plane) angular dependence of the normalized remanent magnetization, M_R/M_S, obtained from VSM loops of a (single) FePt reference layer on MgO(110). Note that this FePt layer has been grown using the same growth parameters as for the FePt in the layer stack investigated in this study.

The Py layer was grown at a high deposition rate, which usually induces disorder and thus results in a low magnetocrystalline anisotropy. However, from the out-of-plane and in-plane XRD spectra in Figs. 4 and 5, respectively, it is clear that the Py layer in our case is also epitaxial. Given its comparably small thickness, this layer could not be selectively investigated with either VSM magnetometry or MOKE. Instead, we studied its behavior via element-selective XMCD measurements on the Ni edge, as shown below.

Finally, the Co layer was deposited using the GLAD process with the intention to achieve a magnetocrystalline easy axis 90° away from the easy axis of the lower hard magnetic FePt layer ($\varphi_{\mathrm{EA}}^{\mathrm{FePt}} = 0^\circ$). To determine the easy

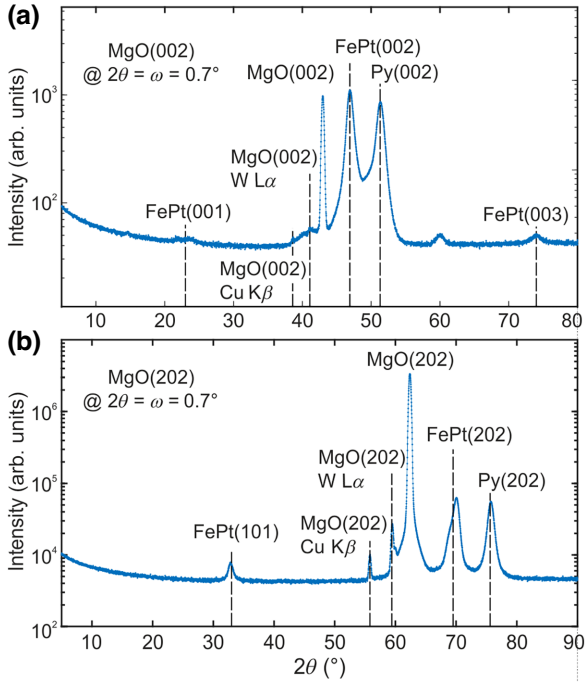

FIG. 5. In-plane ϕ-$2\theta_\chi$ scans with Cu $K\alpha$ radiation and with (a) $\phi = 0$ parallel to the ⟨001⟩ and (b) ⟨101⟩ direction of the MgO substrate, respectively. Note that high and medium resolution was used for the top and bottom scans, respectively.

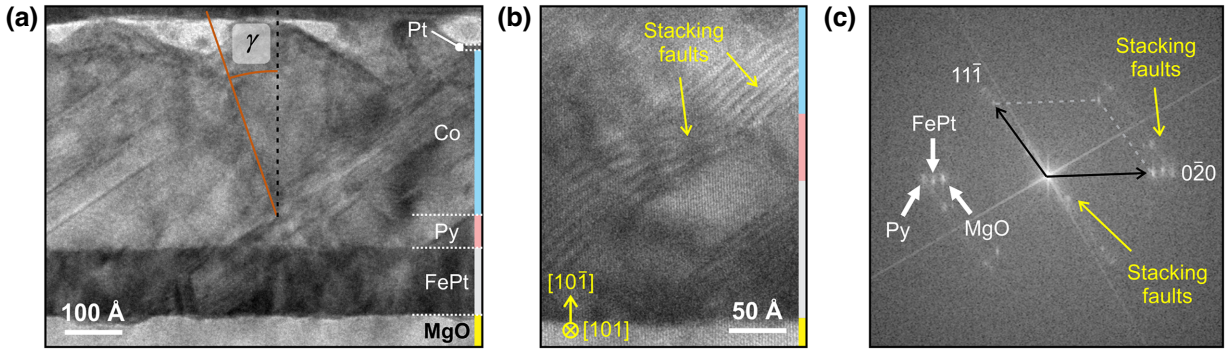

FIG. 6. (a) Bright-field TEM image of the heterostructure, showing an overview of the interfaces. The Co layer, grown via the GLAD process, shows a columnar structure with an inclination angle of approximately 70°. (b) High-resolution TEM image of the MgO/FePt-Py-Co interface regions, showing a high density of stacking faults along the ⟨111⟩ crystalline axis, originating at the FePt/MgO interface and propagating through the subsequent Py and Co layers. (c) Diffractogram [of (b)] showing that the FePt and Py layers are highly epitaxial, following the relationship Py[001](110) ∥ FePt[001](110) ∥ MgO[001](110), and with a high density of stacking faults.

axis of the Co layer, we carried out MOKE measurements of the final layer stack. Given the wavelength and angle of incidence used in the setup, a penetration depth of approximately 300 Å was estimated, which means that the MOKE signal is overwhelmingly due to the upper parts of the Co layer, not affected by the layers and interfaces below. Hysteresis loops were measured at multiple in-plane angles φ_H and the remanent magnetization M_R was extracted from the loops recorded at each in-plane angle to produce the anisotropy plot as shown in Fig. 8. The fit with a model for twofold anisotropy, $M_R/M_S = A|\sin(\varphi_H + \varphi_{HA})| + B$, where A, B, and φ_{HA} are fitting parameters, is shown in red. The fit reveals the easy axis of magnetization at $\varphi_{EA} = 169°$ and the hard axis at $\varphi_{HA+90°} = 79°$, i.e., $\varphi_{EA} = \varphi_{HA} + 90°$. The direction of the easy axis (169°) clearly deviates from the intended 90° orientation, which should be achieved with a deposition angle of $\beta = 0°$, i.e., the imprinting is imperfect.

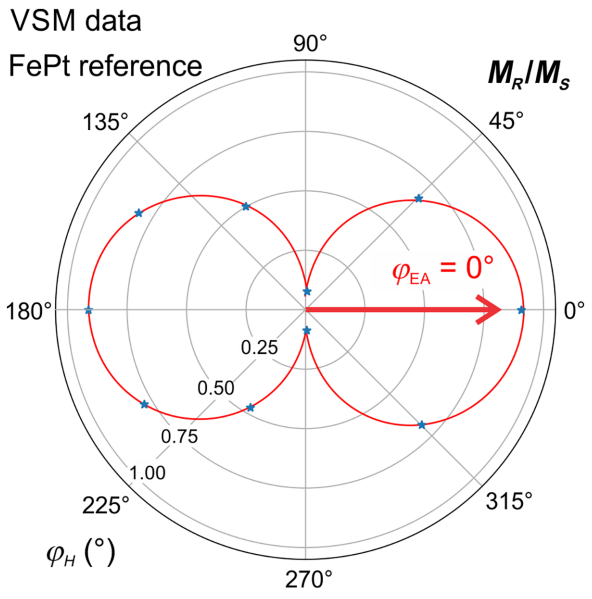

FIG. 7. Anisotropy plot of the normalized remanent VSM magnetization, M_R/M_S, for a FePt reference film on MgO(110). The in-plane angle φ_H is defined relative to the [001] direction of MgO (and FePt). The easy-axis direction, φ_{EA}, obtained from the fit (red curve) to the data is along 0° and shows twofold symmetry.

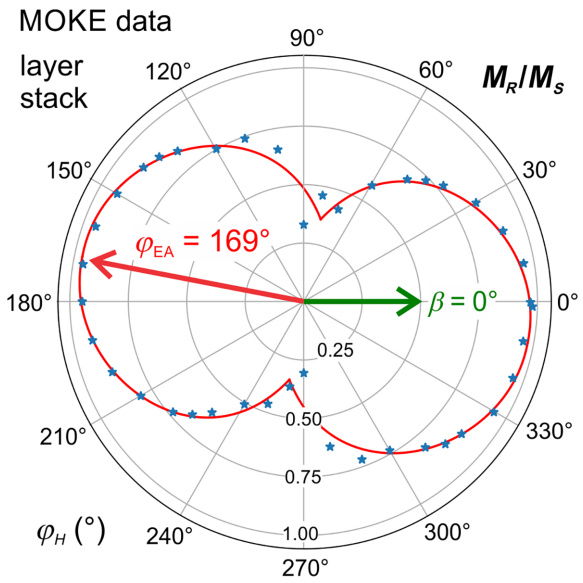

FIG. 8. Anisotropy plot of the normalized remanent MOKE magnetization, M_R/M_S, for the film stack on MgO(110). MOKE is predominantly probing the in-plane anisotropy of the top Co layer, showing a twofold symmetric easy axis oriented along $\varphi_{EA} = 169°$.

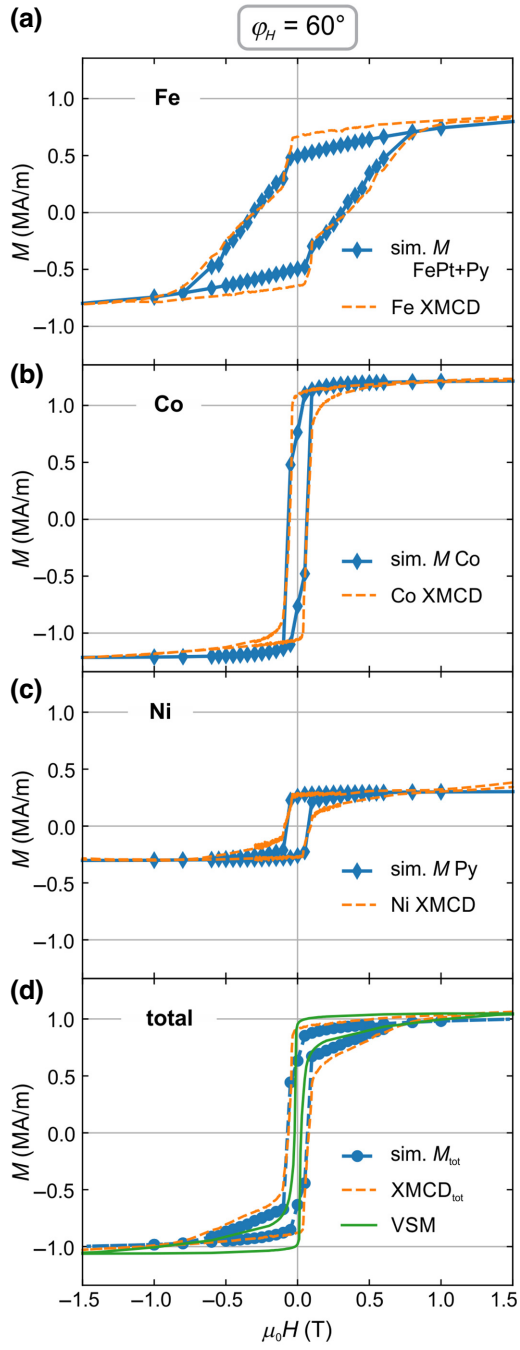

FIG. 9. Elemental XMCD hysteresis loops for (a) Fe, (b) Co, and (c) Ni with the field applied in the $\varphi_H = 60°$ direction (dashed orange line). The results of the micromagnetic simulations are represented by dashed lines (blue diamonds). (d) Plots of the hysteresis loop representative of the behavior of the film stack as a whole, obtained by VSM (green line) and micromagnetic simulations (blue circles). For comparison, the combined XMCD signal is shown as well (dashed orange line), which was obtained by adding the three elemental loops, weighted by their XMCD intensities and volumes.

Owing to this imperfect imprinting of the Co anisotropy, it was not possible to form a measurable ES at remanence. Instead, by applying an in-plane field (here at an angle of

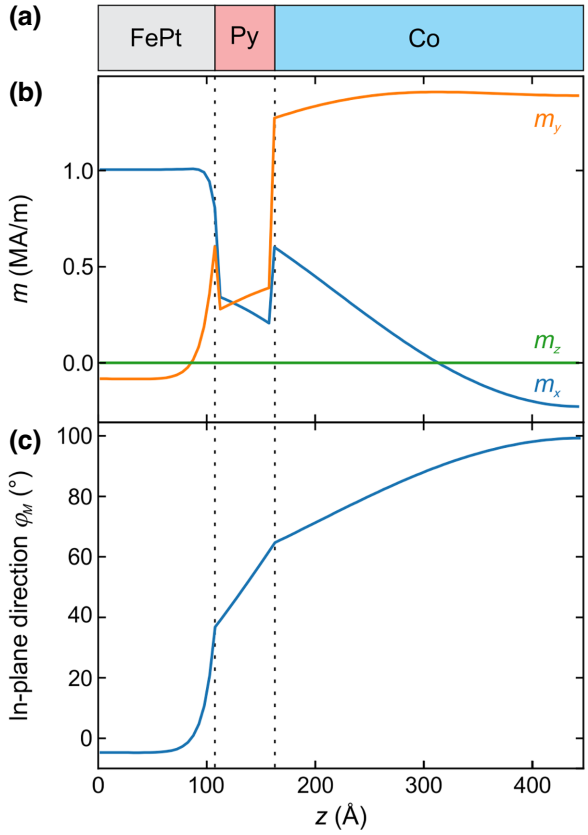

FIG. 10. Simulated magnetic depth profile in zero field (following a hysteresis loop with the field applied in the $\varphi_H = 60°$ direction seen in Fig. 9). (a) FePt/Py/Co layer structure. (b) Depth dependence of the components of the magnetization vector. (c) Plot of the in-plane direction φ_M as a function of depth. The opening angle φ_o is defined as the difference between the two extremal φ_M angles. It is $\varphi_o \approx 105°$ in this case.

$\phi_H = 60°$), the FePt and Co moments are pulled apart since the uniaxial anisotropy fields of the two layers have quite different magnitude. In order to gain insight into the magnetization distribution across the layers, element-selective XMCD was carried out at $\phi_H = 60°$ as shown in Fig. 9 [dashed orange lines for (a) Fe, (b) Co, and (c) Ni]. The XMCD loops for Fe, Co, and Ni are different, while the Co and Ni loops exhibit a distinct square shape. The reader is reminded that the Fe XMCD signal represents a mixed contribution of the FePt and Py layers, while the Ni and Co signals are uniquely revealing the behavior of the Py and Co layers, respectively.

The respective panels in Fig. 9 also show the results of the micromagnetic simulations (blue diamonds) of the hysteresis loops for each layer (where the Fe layer data represents the weighted summation of the FePt and Py layer results). Taking a closer look at the shape of the loops, a two-stage behavior is apparent whereby the first is a steplike transition, followed by a more tail-like transition. This behavior suggests that there are two separate parts

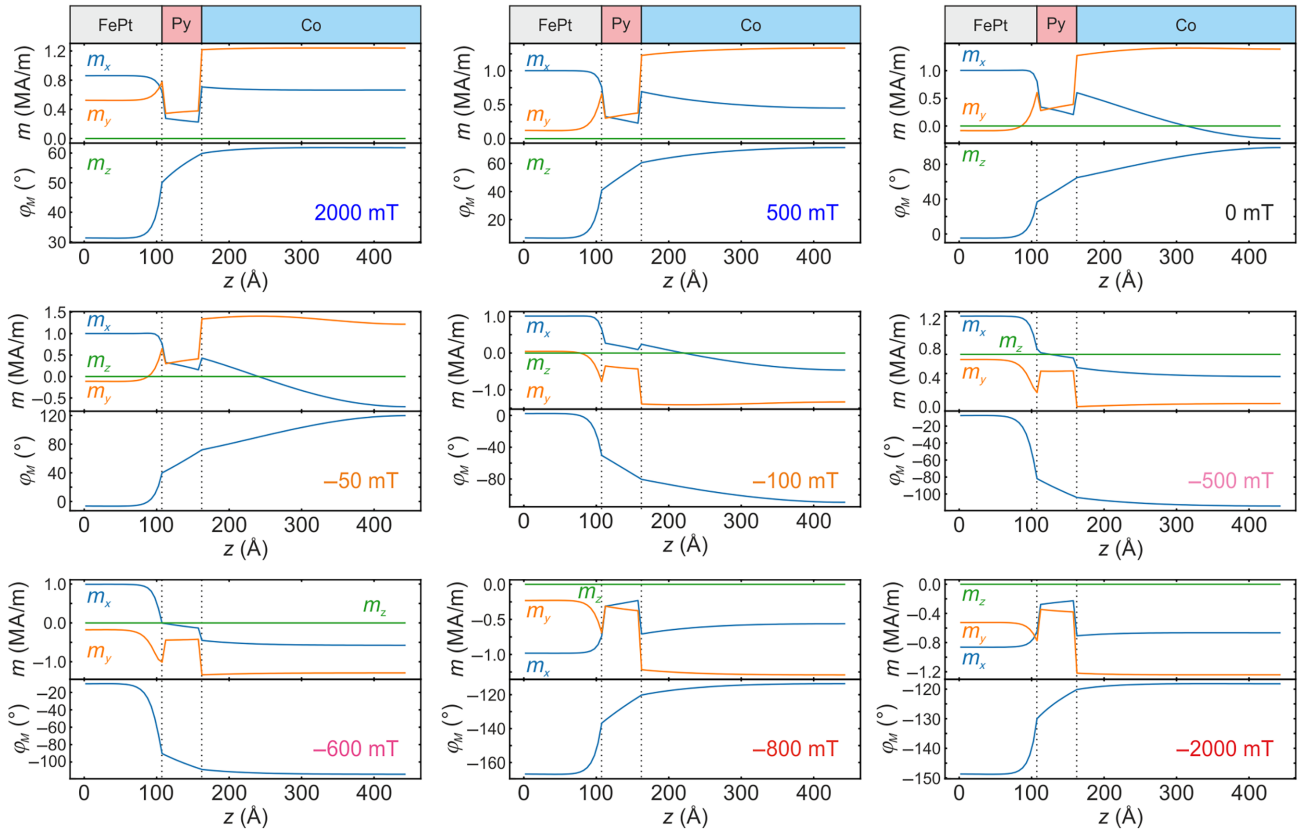

FIG. 11. Simulated magnetic depth profile at decreasing field values, starting at +2000 mT and reaching −2000 mT. The field was applied in the $\varphi_H = 60°$ direction.

of the layer stack which are switching at different applied fields. In common exchange springs, a plateau between the steps is a characteristic feature associated with the formation of an exchange spring [30,31]. In general, in an ES, the soft layer starts to wind at H_{ex}, and the magnetization of the hard layer reverses at H_{irr}. In other words, below H_{irr}, the winding force is large enough to flip the rest of the film and the magnetization is irreversibly switched. Here, the behavior is different in that the first switching field is reached via a step (switching of the soft layer), followed by a continuously changing tail (hard layer following). Note that in order to achieve a hysteresis loop with coercivities corresponding to the measurements the uniaxial anisotropy of FePt and Co had to be 15% and 10% of the common literature values [19], respectively. This is not unreasonable since the long-range order parameter S_{110} for FePt with a value of 0.17 is fairly small (compared to, e.g., 0.81 for an molecular beam epitaxy grown FePt film [22]). In other words, disorder could be the reason for the decrease in anisotropy energy. Disorder could also be the reason for the reduced exchange coupling constant of FePt (10% of the common literature values). One way to increase the coercivity of the film is growth at much higher temperatures, further stabilized by postgrowth annealing [32]. Since the Co layer is likely also disordered, the same argument motivating these smaller values could also apply.

In Fig. 9(d), a comparison with the VSM data for the layer stack as a whole is shown. The intensity of the XMCD spectra, together with the magnetization measured with VSM, was used to scale the respective Fe, Co, and Ni loops, giving the total XMCD curve, which agrees reasonably well with the VSM data, as well as with the micromagnetic simulation results. Figure 10 shows the zero-field magnetic depth profiles corresponding to the simulated results shown in Fig. 9. As can be seen in the simulated magnetic depth profiles, a magnetic ES can be induced at zero field.

The magnetic depth profiles were also simulated at other field points in the hysteresis loop (see Fig. 9) with the field ranging from +2 to −2 T (applied along $\varphi_H = 60°$), as shown in Fig. 11. They show that an ES is present for all fields, with varying in-plane opening angle φ_o (defined as the difference between the extremal FePt and Co angles). From 2 T down to zero field, the opening angle of the spring increases from $\varphi_o \approx 30°$ to 105° at zero field [see Fig. 10(c)]. The Co layer makes an abrupt 90° switch to align with the applied field between −0.05 and −0.1 T (as can be seen in the orange m_y component changing from its full value to almost zero), accompanied by a switching

of the direction of the spring. From −0.1 to −0.6 T, the winding in the Co layer decreases while the winding of the FePt layer increases, whereas φ_o remains unchanged. This behavior corresponds to the long tail observed in Fig. 9. Between −0.6 and −0.8 T, the FePt layer makes a 180° switch to align with its easy axis direction, which means that it is still not aligned with the applied field. This behavior is similar to the jump in the Co layer (−0.05 and −0.1 T) and can be seen in the m_x component inverting sign, again accompanied by a switching of the direction of the spring. Finally, a further increase of the (negative) field rotates the FePt moments to the direction of the applied field until $\varphi_o \approx 30°$ at 2 T (ultimately reaching 0° at very high fields). To summarize the simulations, it appears that there is always an ES set up between the Co and FePt layers. The experimental observed two-stage switching behavior, i.e., a step and a long tail, corresponds to the switching of the Co and the winding of the FePt, respectively. Before the Co layer switches, varying the field changes the in-plane direction φ_o, while it remains constant after Co switched, now transferring the winding from the Co to the Pt layer.

In contrast to the intended materials design specifications [as illustrated in Fig. 1(e)], the ES is not confined to the Py layer, but all three layers, including the FePt layer, are wound to some degree. Nevertheless, such ES structures are very promising from the point of view of optical and microwave-induced control of the magnetization [33]. Also, this behavior bears some resemblance with the behavior of continuously graded magnetic multilayer systems [34], i.e., systems which have an engineered compositional depth profile. This distributed interface between the hard and soft layers has been shown to be advantageous for the exchange spring behavior [35,36]. As mentioned above, one way to improve the response of the system is to increase the magnetocrystalline anisotropy of the FePt by high-temperature growth and postannealing [32]. This way, the ES would not extend into the FePt layer. Next, the growth of the Py should be optimized, yielding a more disordered film with very low magnetocrystalline anisotropy. Note that since the FePt and Py layers were not exhibiting the desired properties, a thicker Co layer was required to achieve overall ES behavior. This increase in thickness resulted in its easy axis moving away from the GLAD-imprinted 90° orientation.

IV. CONCLUSION

In conclusion, an exchange spring system in zero applied field has been realized, while a larger winding angle can be obtained through the application of a magnetic field. As the hard magnetic bottom and top layers, magnetron-sputtered FePt and Co films, respectively, were used which exhibit different in-plane anisotropies. Whereas the anisotropy of the FePt layer was governed by epitaxy, the Co layer was engineered using GLAD. However, while the goal was to wind up the moments in the intermediate Py layer only, due to its epitaxial growth and resulting loss in anisotropy in the Co layer, the ES extended across all three layers. While this behavior is not ideal, our work nevertheless demonstrates the basic concept of using GLAD to engineer the anisotropy of one of the hard magnetic layers, making the heterostructure very promising for optical and microwave-induced control of magnetization. Future work will be dedicated to improving on the layer properties within the heterostructure.

ACKNOWLEDGMENTS

The authors acknowledge the Engineering and Physical Sciences Research Council (EPSRC) under Grants No. EP/P021190/1, No. EP/P020151/1, No. EP/P02047X/1, and No. EP/N032128/1. The work of D.G.N. was supported by the EPSRC Centre for Doctoral Training in Metamaterials under Grant No. EP/L015331/1. We would like to thank Gavin Stenning and Daniel Nye for their help with the Rigaku SmartLab and the NanoMOKE in the Materials Characterisation Laboratory at the ISIS Neutron and Muon Source, and Marijan Beg for introducing us to Ubermag. Diamond Light Source is acknowledged for access and support in use of the electron Physical Science Imaging Centre (Instrument E02 proposals MG23285-77 & 78), and for provision of beamtime on beamline I10 under proposal MM23338, and we thank Alpha N'Diaye for assistance during experiments on beamline 6.3.1 at the Advanced Light Source, Berkeley, USA.

[1] E. F. Kneller and R. Hawig, The exchange-spring magnet: A new material principle for permanent magnets, IEEE Trans. Magn. **27**, 3588 (1991).

[2] S. Li, B. Livshitz, H. N. Bertram, E. E. Fullerton, and V. Lomakin, Microwave-assisted magnetization reversal and multilevel recording in composite media, J. Appl. Phys. **105**, 07B909 (2009).

[3] W. Zhou, T. Yamaji, T. Seki, H. Imamura, and K. Takanashi, Resonant magnetization switching conditions of an exchange-coupled bilayer under spin wave excitation, Appl. Phys. Lett. **110**, 082401 (2017).

[4] T. Seki, K. Utsumiya, Y. Nozaki, H. Imamura, and K. Takanashi, Spin wave-assisted reduction in switching field of highly coercive iron-platinum magnets, Nat. Commun. **4**, 1726 (2013).

[5] T. Seki, W. Zhou, and K. Takanashi, Resonant switching for an in-plane magnetized $L1_0$-FePt|$Ni_{81}Fe_{19}$ bilayer under spin wave excitation, J. Phys. D: Appl. Phys. **49**, 075002 (2016).

[6] M. M. Hawkeye and M. J. Brett, Glancing angle deposition: Fabrication, properties, and applications of micro- and nanostructured thin films, J. Vac. Sci. Technol. A **25**, 1317 (2007).

[7] A. Frisk, B. Achinuq, D. G. Newman, E. Heppell, M. Dąbrowski, R. J. Hicken, G. van der Laan, and T. Hesjedal, Controlling in-plane magnetic anisotropy of Co films on MgO substrates using glancing angle deposition, Phys. Status Solidi A **220**, 2300010 (2023).

[8] K. Ozawa, T. Yanada, H. Masuya, M. Sato, S. Ishio, and M. Takahashi, Oblique incidence effects in evaporated iron thin films, J. Magn. Magn. Mater. **35**, 289 (1983).

[9] K. Schlage, L. Bocklage, D. Erb, J. Comfort, H.-C. Wille, and R. Röhlsberger, Spin-structured multilayers: A new class of materials for precision spintronics, Adv. Funct. Mater. **26**, 7423 (2016).

[10] M. Ohtake, A. Itabashi, F. Kirino, and M. Futamoto, $L1_0$ Ordered FePd FePt, and CoPt thin films with flat surfaces prepared on MgO(110) single-crystal substrates, IEEE Trans. Magn. **49**, 3295 (2013).

[11] M. Kateb, J. T. Gudmundsson, and S. Ingvarsson, Effect of atomic ordering on the magnetic anisotropy of single crystal $Ni_{80}Fe_{20}$, AIP Adv. **9**, 035308 (2019).

[12] M. Björck and G. Andersson, GenX: An extensible x-ray reflectivity refinement program utilizing differential evolution, J. Appl. Crystallogr. **40**, 1174 (2007).

[13] G. van der Laan and A. I. Figueroa, X-ray magnetic circular dichroism—a versatile tool to study magnetism, Coord. Chem. Rev. **277–278**, 95 (2014).

[14] L. B. Duffy, A. Frisk, D. M. Burn, N.-J. Steinke, J. Herrero-Martin, A. Ernst, G. van der Laan, and T. Hesjedal, Imposing long-range ferromagnetic order in rare-earth-doped magnetic topological-insulator heterostructures, Phys. Rev. Mater. **2**, 054201 (2018).

[15] M. Beg, R. A. Pepper, and H. Fangohr, User interfaces for computational science: A domain specific language for OOMMF embedded in Python, AIP Adv. **7**, 056025 (2017).

[16] M. Beg, R. A. Pepper, T. Kluyver, J. Mulkers, J. Leliaert, and H. Fangohr, Ubermag: Meta package for Ubermag project (accessed: 24 July 2022, 2019).

[17] M. Beg, M. Lang, and H. Fangohr, Ubermag: Toward more effective micromagnetic workflows, IEEE Trans. Magn. **58**, 7300205 (2022).

[18] https://ubermag.github.io/documentation/notebooks/micromagneticmodel/energy-terms.html (accessed: 8 September 2023).

[19] J. M. D. Coey, *Magnetism and Magnetic Materials* (Cambridge University Press, Cambridge, 2010).

[20] T. Kojima, M. Ogiwara, M. Mizuguchi, M. Kotsugi, T. Koganezawa, T. Ohtsuki, T.-Y. Tashiro, and K. Takanashi, Fe-Ni composition dependence of magnetic anisotropy in artificially fabricated $L1_0$-ordered FeNi films, J. Phys.: Condens. Matter **26**, 064207 (2014).

[21] R. F. C. Farrow, D. Weller, R. F. Marks, M. F. Toney, A. Cebollada, and G. R. Harp, Control of the axis of chemical ordering and magnetic anisotropy in epitaxial FePt films, J. Appl. Phys. **79**, 5967 (1996).

[22] R. F. C. Farrow, D. Weller, R. F. Marks, M. F. Toney, D. J. Smith, and M. R. McCartney, Magnetic anisotropy and microstructure in molecular beam epitaxial FePt(110)/MgO(110), J. Appl. Phys. **84**, 934 (1998).

[23] T. Seki, T. Shima, K. Takanashi, Y. Takahashi, E. Matsubara, and K. Hono, Optimum compositions for the low-temperature fabrication of highly ordered FePt [001] and FePt [110] films, IEEE Trans. Magn. **40**, 2522 (2004).

[24] T. Seki, T. Shima, and K. Takanashi, Fabrication of in-plane magnetized FePt sputtered films with large uniaxial anisotropy, J. Magn. Magn. Mater. **272–276**, 2182 (2004).

[25] T. Seki, T. Shima, K. Yakushiji, K. Takanashi, G. Q. Li, and S. Ishio, Dot size dependence of magnetic properties in microfabricated $L1_0$-FePt (001) and $L1_0$-FePt (110) dot arrays, J. Appl. Phys. **100**, 043915 (2006).

[26] T. Shima, K. Takanashi, Y. K. Takahashi, and K. Hono, Coercivity exceeding 100 kOe in epitaxially grown FePt sputtered films, Appl. Phys. Lett. **85**, 2571 (2004).

[27] B. Laenens, F. Almeida, A. Vantomme, and J. Meersschaut, Determination of the direction of the *c*-axis of $L1_0$ FePt thin films with the Mössbauer spectroscopy, Acta Phys. Pol. A **112**, 1313 (2007).

[28] M. Birkholz, *Thin Film Analysis by X-Ray Scattering* (Wiley-VCH, Weinheim, 2006).

[29] J. M. Nieuwenhuizen and H. B. Haanstra, Microfractography of thin films, Philips Tech. Rev. **27**, 87 (1966).

[30] E. E. Fullerton, J. S. Jiang, M. Grimsditch, C. H. Sowers, and S. D. Bader, Exchange-spring behavior in epitaxial hard/soft magnetic bilayers, Phys. Rev. B **58**, 12193 (1998).

[31] T. A. Taaev, K. S. Khizriev, and A. K. Murtazaev, Monte Carlo study of magnetization reversal in the model of a hard/soft magnetic bilayer, J. Exp. Theor. Phys. **124**, 924 (2017).

[32] K. Son, G. Ryu, H.-H. Jeong, L. Fink, M. Merz, P. Nagel, S. Schuppler, G. Richter, E. Goering, and G. Schütz, Superior magnetic performance in FePt L10 nanomaterials, Small **15**, 1902353 (2019).

[33] M. Dabrowski, A. Frisk, D. M. Burn, D. G. Newman, C. Klewe, A. T. N'Diaye, P. Shafer, E. Arenholz, G. J. Bowden, T. Hesjedal, G. van der Laan, G. Hrkac, and R. J. Hicken, Optically and microwave-induced magnetization precession in [Co/Pt]/NiFe exchange springs, ACS Appl. Mater. Interfaces **12**, 52116 (2020).

[34] L. Fallarino, B. J. Kirby, and E. E. Fullerton, Graded magnetic materials, J. Phys. D: Appl. Phys. **54**, 303002 (2021).

[35] J. S. Jiang, J. E. Pearson, Z. Y. Liu, B. Kabius, S. Trasobares, D. J. Miller, S. D. Bader, D. R. Lee, D. Haskel, G. Srajer, and J. P. Liu, A new approach for improving exchange-spring magnets, J. Appl. Phys. **97**, 10K311 (2005).

[36] M. Quintana, A. Meléndez, C. Martín Valderrama, L. Fallarino, and A. Berger, Temperature-independent coercivity in compositionally graded ferromagnetic multilayers, Phys. Rev. Appl. **18**, 054024 (2022).